

The ODU CAS Inverse Compton Source Design

K. Deitrick, J. Delayen, R. Gamage, K. Hernandez,
C. Hopper, G. Krafft, R. Olave, and T. Satogata*
Old Dominion University

September 5, 2013

Abstract

A compact electron accelerator suitable for Compton source applications is in design at the Center for Accelerator Science at Old Dominion University. The design includes a KE=1.55 MeV low-emittance, optimized superconducting 500 MHz electron gun; a 25 MeV linac with multi-spoke 4.2 K 500 MHz superconducting RF cavities; and transport that combines magnetic longitudinal bunch compression and transverse final focus. This white paper summarizes initial designs of each element, including end to end simulations with ASTRA and elegant, expected beam parameters, and cryogenic heat load considerations. The initial design of this electron accelerator was presented in [1].

1 Design Parameters

A Compton source is essentially a lepton-photon collider. The total number of source photons produced per bunch crossing is

$$N_x = \frac{N_e N_\gamma}{2\pi \sqrt{\sigma_{e,x}^2 + \sigma_{\gamma,x}^2} \sqrt{\sigma_{e,y}^2 + \sigma_{\gamma,y}^2}} \sigma_T \quad (1.1)$$

where N_e is the number of electrons per bunch, N_γ is the number of photons per bunch, $\sigma_T \equiv 8\pi r_e^2/3$ is the Thomson cross section, r_e is the classical electron radius, and the sigmas represent the RMS beam sizes of the electron and photon beams at the interaction point in the two transverse directions. Implicit in this calculation is that the electron bunch length is smaller than the beta-function, so that flux reduction due to the hourglass effect is minimized. The flux of photons produced is $F = f N_x$ where f is the collision repetition frequency; multiply this by 1.5×10^{-3} to obtain the flux into a 0.1% bandwidth in the forward direction [2].

The energy of the photons emerging in the forward direction is given by a modified FEL resonance condition

$$E_\gamma \sim 4\gamma^2 E_{\text{laser}} \quad (1.2)$$

The extra factor of two compared to the undulator result is present because the laser-photon-based undulator is itself moving at the velocity of light in the lab frame. Usually for FEL applications, the RMS emittance required from the electron beam source is given by the requirement to achieve the diffraction limit

$$\epsilon < \frac{l}{4\pi} \quad (1.3)$$

where l is the wavelength of the emitted radiation. In general, this limit cannot be achieved in Compton sources as the beam energy is lower than in light sources and therefore the rms emittance is quite a bit larger. The brightness of the source in the non-diffraction limited mode of operation is

$$B = F/(4\pi^2 \epsilon_x \epsilon_y) \quad (1.4)$$

*Email: tsatogat@odu.edu

Therefore, to obtain maximum photon brightness, minimum transverse emittance is desirable; the electron beam spot may also be made smaller in collision.

The electron beam requirements for the longitudinal degree of freedom are also easily determined by the photon beam requirements. The constraint that energy smearing of the forward flux is small compared to the total bandwidth requires that the compressed beam energy spread be less than 0.03%. At 25 MeV this translates to 7.5 keV. Ideally, the bunch length is compressed to around 1 mm to make the flux reduction from the hourglass effect insignificant. Thus we should be planning for a longitudinal phase space of around 7.5 eV-m or smaller.

This requirement is smaller than, but reasonably close to, what one might expect from an SRF gun and injector system. The following table, based on the MIT parameter tables [3], provides a self-consistent set of goal parameters [4].

Parameter	Quantity	Units
Energy	25	MeV
Bunch charge	10	pC
Repetition rate	100	MHz
Average current	1	mA
Transverse normalized emittance	0.1	mm-mrad
$\beta_{x,y}$	5	mm
FWHM bunch length	3.0 (0.9)	psec (mm)
RMS energy spread	7.5	keV

Table 1: Electron Beam Parameters at Collision

Parameter	Quantity	Units
Wavelength	1 (1.24)	μm (eV)
Circulating Power	1	MW
N_γ , Number of photons/bunch	5×10^{16}	
Spot size	3.2	μm
Peak strength parameter, $a = \frac{eEl}{2\pi mc}$ [2]	0.026	

Table 2: Optical Cavity Parameters

Parameter	Quantity	Units
X-ray energy	Up to 12	keV
Photons/bunch	1.6×10^6	
Flux	1.6×10^{14}	photon/sec
Average brilliance	1.5×10^{15}	photon/(sec-mm ² -mrad ² -0.1%-BW)

Table 3: Compton Source Parameters

2 Electron Gun

2.1 Design and Optimization

The quarter-wave gun developed and tested by Harris et al. [5] from the Naval Postgraduate School in collaboration with Niowave, Inc, was used as the starting point for the geometric design of the electron source cavity. This is a highly reentrant cavity, with a length on the order of $\lambda/4$, where λ is the longest

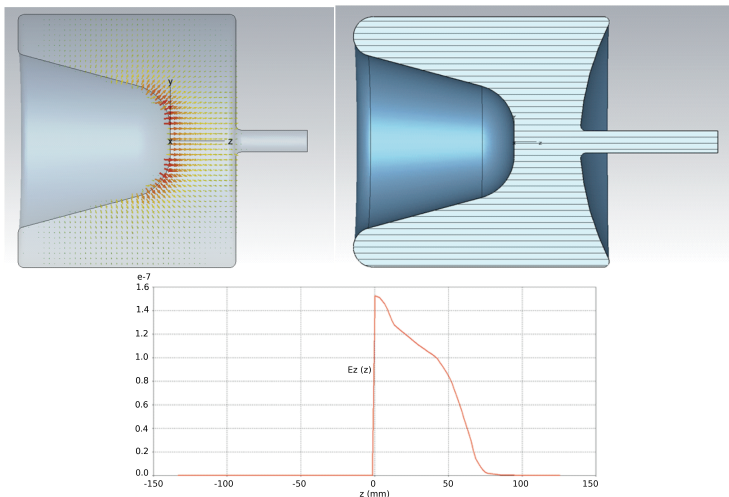


Figure 1: Geometries under consideration for the 500 MHz quarter-wave electron gun. The left geometry and field profile below are for the original Harris gun. Initial optimization led to a reentrant cavity with a spherical inward curvature at the beam exit face, pictured on the right.

Parameter	Value	Units
Longitudinal distribution	Plateau	
Bunch length	24	ps
Rise time	6	ps
RMS bunch radius	0.5	mm
Bunch charge	10	pC
Initial kinetic energy	1	keV
p_z distribution	Isotropic	

Table 4: Parameters of Electron Bunch Produced by the Cathode

resonant wavelength of the cavity. Fig. 1 shows the initial design and the electric field established in the cavity on the left, as well as the accelerating field profile along the beamline. Since this quarter-wave gun is developed for compact light sources, an RF frequency of 500 MHz was chosen to allow for a compact cavity size. Initial design alterations and optimization were performed with CST Microwave Studio[®] 2012 (CST) [6]. Due to increasing concerns about how CST handles curves and the resulting ambiguity of the gun geometry, further design alteration was handled by Superfish, version 7.19, developed by the Los Alamos Accelerator Code Group [7].

Using the ASTRA (A Space-charge TRacking Algorithm) code developed at DESY [8], version 3.0, we performed a particle-tracking simulation of this quarter wave gun using as input the electromagnetic RF fields found by CST. Details of these simulations are covered in Section 5.1. We tracked 500 electrons with a total charge of 10 pC, in a distribution described in Table 4, including space-charge effects, for 0.15 m, well beyond the gun exit iris. ASTRA automatically determines a particle phase that optimizes the coupling with the RF fields, so a particle phase of 0° has maximum energy gain. The results indicated that an electron beam traversing the preliminary cavity would be divergent. An additional design constraint was added,

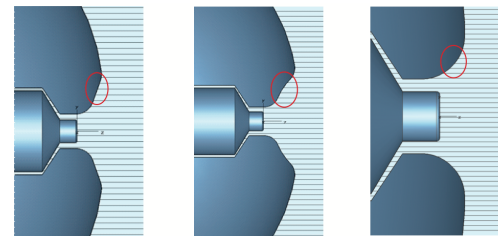


Figure 2: Variations on the cathode aperture geometry: (A) flat, (B) concave, (C) convex.

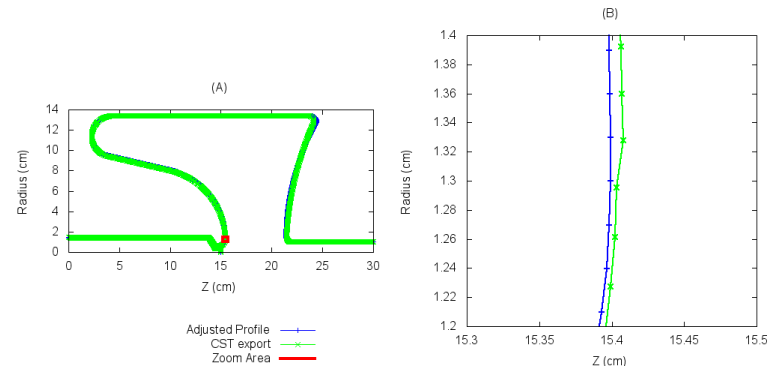


Figure 3: Geometric comparisons of adjusted profile and CST exported profile. (A) Overview of entire gun profile; (B) Zoom area of surface tangent discontinuity.

so that the geometry of the nosecone containing the cathode resulted in minimal-divergent or convergent beams. We explored three different variations of nosecone aperture curvature, with a flat, concave or convex aperture, as shown in Fig. 2.

From the results given by ASTRA, we determined that the only cavity geometry suitable for our application has a convex-shaped nosecone reentrance geometry. Preliminary studies without the cathode had pointed to the a reentrant cavity with a spherical inward curvature on the beam exit face as the most suitable for optimization. Likewise, our conclusion after considering the different parameters sweeps and different cavity geometries in CST, is that in general this cavity performed better than the other geometries in terms of low surface fields and high shunt impedance.

The design was then implemented using Superfish to automate a more thorough gun optimization and, eventually, an optimization of the entire system. When CST exported the geometry of the gun cross section, however, the geometry did not recreate the same results in Superfish. It became clear that while CST would address surface tangent discontinuities where two curves met, these discontinuities were not reliably exported. If the exported geometry was reimported to CST, the results would not be reproduced. Specifically for the gun in question, the exported geometry suffered from a surface tangent discontinuity where the blend of the nosecone intersects the blend of the nosecone aperture. This intersection, indicated by the red box of the left plot in Fig. 3, shows both this discontinuity and the adjusted version that eliminates it.

While this may seem insignificant, Fig. 4 compares the resulting fields of the two geometries, both generated by Superfish. These fields were generated along a path parallel to the beamline, but radially

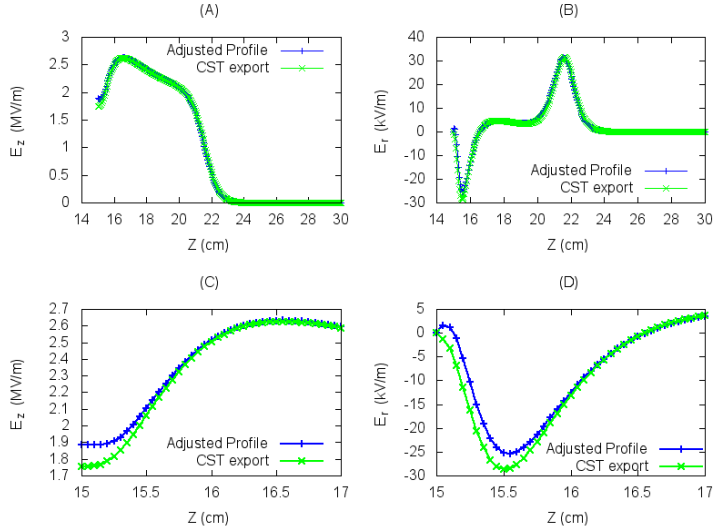


Figure 4: Field differences between adjusted profile and CST export. (A) Longitudinal electric field along path parallel to beam axis at radius of 0.5 mm; (B) Radial electric field along path parallel to beam axis at radius of 0.5 mm; (C) First 2 cm of (A); (D) First 2 cm of (B).

displaced by 0.5 mm, the RMS radius of the bunch distribution off of the cathode. While the top row compares the longitudinal and radial fields across the entire cavity, the bottom row compares these fields for the first two centimeters. At the end of the first two centimeters $\beta = 0.86$, making this region very significant in terms of space charge effects, which has consequences further down the beam line.

Fig. 5 shows the preliminary design based on the initial parameter sweeps performed in CST and finalized in Superfish. This is a reentrant cavity with a spherical inward curvature on the beam exit face, and a convex nosecone aperture. This figure also presents the electric field profile along the beamline of the fundamental accelerating mode, and cut-views of the cavity's surface electric and magnetic fields. Tables 5 and 6 present the cavity's geometric and RF properties, respectively. The RF parameters have been presented at both $E_0 = 1$ MV/m, which Superfish uses for postprocessing, and the operating gradient of the gun, $E_0 = 10.6$ MV/m.

2.2 Tracking

Fig. 6 presents the particle distribution at $z=0$ m and $z=0.15$ m as tracked in ASTRA. Fig. 7 presents the phase space results given by ASTRA for the particles at $z=0.15$ m. This distribution was consequently tracked through a number of spoke cavities, to design the linac, which is covered in Section 5.1. The determination of the operating gradient is addressed in that section, due to the dependence of the linac on the gun. Also addressed there is the lack of emittance compensation and the reasoning behind that decision.

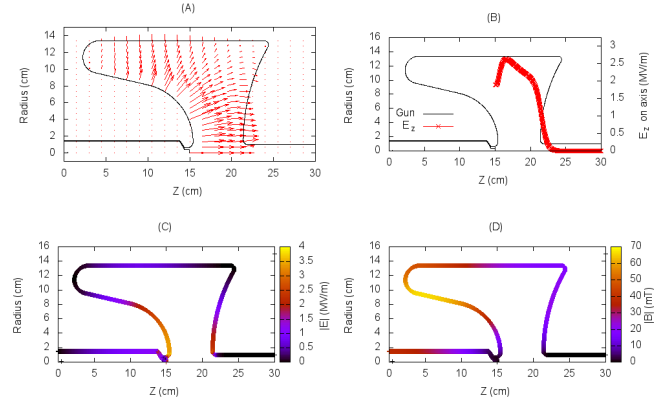


Figure 5: Preliminary design of a 500 MHz quarter wave electron gun. (A) Longitudinal cross section and electric field within the cavity at $E_0 = 1$ MV/m; (B) Accelerating electric field profile along beam axis; (C) Surface electric field; (D) Surface magnetic field.

Parameter	Value	Units
Length of gun (excluding cathode holder and exit pipe)	221.46	mm
Radius of gun	133.94	mm
Length of cathode to iris	69.0	mm
Length of iris to maximum exit face	25.0	mm
Radius of reentrance sphere at exit face	226.37	mm
Radius of spherical blends on exit face	5.0	mm
Radius of exiting beampipe	10.0	mm
Angle of nosecone	13.0	degrees
Radius of spherical nosecone blend	70.0	mm
Radius of spherical nosecone aperture blend	7.0	mm
Recess of cathode in nosecone	4.0	mm
Radius of blend between front face and cavity side wall	20.0	mm
Radius of blend between nosecone and front face	18.743	mm

Table 5: Physical Geometry of the 500 MHz Quarter Wave Electron Gun

3 Linac

3.1 SRF Design Parameters

Accelerating electrons near the speed of light has, to date, not been pursued with multi-spoke cavities. This is mainly due to the successful performance of TM-type cavities. Multi-spoke cavities are well-known options for acceleration of heavy and light ions. Our studies of multi-spoke cavities for $v \approx c$ ($\beta_0 \approx 1$) indicate that they are an attractive option for electron accelerators as well [9, 10, ?, 12, 13].

A radio frequency (RF) structure which is suitable for electron acceleration in a compact light source must meet several criteria. 1) The structure must be as compact as possible, 2) the structure must impart several MV to the beam in a single cavity, 3) the power consumption must be low enough to be compatible with 4.2 K operation, and 4) the structure must be able to maintain a high beam quality while accelerating

Parameter	Value at		Units
	$E_0 = 1 \text{ MV/m}$	$E_0 = 10.6 \text{ MV/m}$	
Frequency of accelerating mode		499.3	MHz
$\lambda/4$		150	mm
Design β		0.95	
Stored Energy	44		mJ
QR_s		83.5	Ω
R/Q		154	Ω
Average kinetic energy gain	0.15	1.554	MeV
Maximum accelerating voltage on-axis	2.631	27.972	MV/m
Peak electric surface field (E_p)	3.670	39.02	MV/m
Peak magnetic surface field (B_p)	6.64	70.63	mT
E_p/B_p		1.810	mT/(MV/m)

Table 6: RF Properties of the 500 MHz Quarter Wave Electron Gun

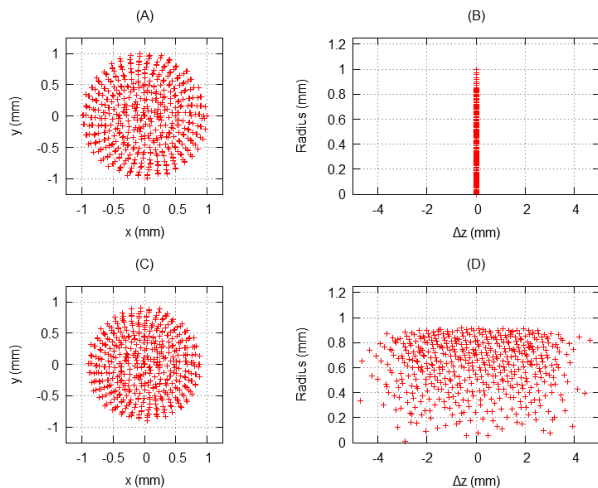


Figure 6: (A) Beam spot off of cathode; (B) Longitudinal distribution off of cathode; (C) Beam spot at gun exit; (D) Longitudinal distribution at gun exit.

the beam from the electron gun to the bunch compression system.

Spoke resonators meet criteria (1) as they have a smaller transverse cross section (for a given frequency) than their TM-type counterparts. In addition to the relatively small transverse dimensions, these cavities have the capability of attaching higher order mode (HOM) and power couplers to the outer conductor rather than in between cavities along the beam pipe, which reduces the longitudinal dimensions (i.e. increases the real estate gradient). An accelerating voltage of 6 MV in a single cavity at 4.2 K is expected with a peak electric field of 25 MV/m and peak magnetic field of 51 mT, which satisfies criteria (2). A low energy content requires less power to overcome microphonics while a high shunt impedance reduces power dissipation, which both contribute to achieving criteria (3). Finally, as will be shown in a later section, beam transport simulations have shown that the beam quality remains almost unchanged while traversing through

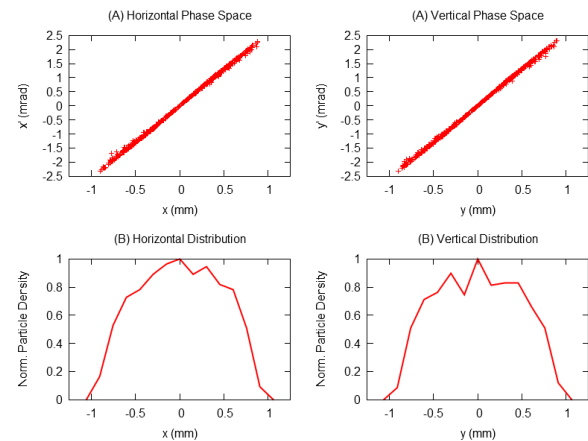


Figure 7: Results from ASTRA of the particle phase space at $z = 0.15 \text{ m}$. (A) Transverse momentum (p_x or p_y) vs longitudinal momentum (p_z) in the transverse (x or y) direction. (B) Normalized particle density vs transverse (x and y) distribution.

Parameter	Value	Units
Average kinetic energy	1.554	MeV
Energy spread	0.4720	keV
Transverse beam emittance x	0.0679	$\pi \text{ mm-mrad}$
Correlated divergence x	1.163	mrad
Transverse beam emittance y	0.0670	$\pi \text{ mm-mrad}$
Correlated divergence y	1.177	mrad
Longitudinal beam emittance z	0.843	$\pi \text{ keV-mm}$

Table 7: Results at $z = 0.15 \text{ m}$ from the Tracking Simulation in ASTRA

an even number of cavities with alternating spoke orientation, thus meeting criteria (4).

Because the spoke cavity has a smaller cross section than a TM (at the same frequency), the spoke can be designed for lower frequencies with longer gaps, and lower BCS cryogenic losses. Frequencies of 500 MHz and below allow for 4.2 K operation. It is the combination of manageable size and 4.2 K operations which led us to the choice of 500 MHz. We also have spoke cavity designs for 325 MHz and 352 MHz which have reduced cryogenic power consumption at the expense of larger cavity (and thus cryostat) size, but this white paper concentrates on the 500 MHz design that was developed in [14] and [15].

The results presented in this section were obtained using CST [6]. This package is well suited for designing and modeling of complex geometries and allows for the full three-dimensional field data to be exported for beam simulation studies, HOM analysis [16], multipacting simulations [17], and magnetic multipole evaluation [?].

The primary goal in optimizing the cavity was to minimize the peak surface electric and magnetic fields for a given accelerating voltage while maximizing the shunt impedance. The former goal requires large spoke, especially in the region where they meet the outer conductor. This has the adverse effect of increasing the cavity diameter in order to compensate for the increase in frequency that larger spokes lead to. Tables 8 and 9 present some of the physical and RF properties of an optimized cavity design.

Parameter	Value	Units
Frequency of accelerating mode	500.006	MHz
Frequency of nearest mode	507.1	MHz
Cavity diameter	416.4	mm
Iris-to-iris length	725	mm
Cavity length	805	mm
Reference length $[(3/2)\beta_0\lambda]$	900	mm
Aperture diameter	50	mm

Table 8: Cavity Parameters, 500 MHz, $\beta_0 = 1$

Parameter	Value	Units
Energy Gain* at β_0	900	kV
R/Q	675	Ω
QR_s	174	Ω
$(R/Q)\times QR_s$	1.2×10^5	Ω^2
E_p/E_{acc}	3.7	-
B_p/E_{acc}	7.6	mT/(MV/m)
B_p/E_p	2.05	mT/(MV/m)
Energy Content*	0.38	J
Power Dissipation*	0.87	W

At $E_{acc} = 1$ MV/m and reference length $(3/2)\beta_0\lambda$
* $R_s = 125$ n Ω

Table 9: RF Properties, 500 MHz, $\beta_0 = 1$

Fig. 8 shows the peak surface electric and magnetic fields. Since the electric field is concentrated along the beam line, the peak surface electric field is in that area. Similarly, the magnetic field encircles the spokes, so as expected, the peak surface magnetic field occurs near the spoke/outer conductor interface.

The fundamental, accelerating mode of the spoke resonator is a π -mode, where the field changes sign from cell to cell, as can be seen in Fig. 9.

3.2 Cryogenic Requirements

The requirements for the helium refrigerator system are based on conservative assumptions. At the operating voltage of 6 MV, the dynamic load is estimated to be around 37.5 W per cavity and 25 W for the electron gun, totaling 175 W. Thermal radiation and conduction through the supports, coupler/cleaning ports, and beam port are responsible for the static load. It is expected that the input and pickup couplers could be located on the outer cylinder, perpendicular to one of the spokes (as shown in Fig. ?? (b)), where the magnetic field is very low. In this way, the contribution to the static load can be minimized. Additionally, for the cleaning and beam ports (located on the end caps), the power dissipation is small, and expected to be less than 1 W for all ports combined.

The helium refrigerator system, which can support 4.2 K operation at load, requires a numbers of components and subsystems. Some assumptions are being made concerning the operation. We will first assume 8 hr/day, 5 days/week, and 52 weeks/year operation. The liquid He static losses are continuous. The number of cavities will play a role in the static losses, and they will be proportional to $1/f_0$. Based on experience at Jefferson Lab [19, 20], a 4.4 K Cryo-plant of 400 W would be \$5M (including injector). This may be an overestimate, since we need only 300 W capacity. The power supply distribution will be assumed at \$60/W. A 50% RF power supply efficiency will also be assumed.

A complete cost estimation and optimization remains to be conducted.

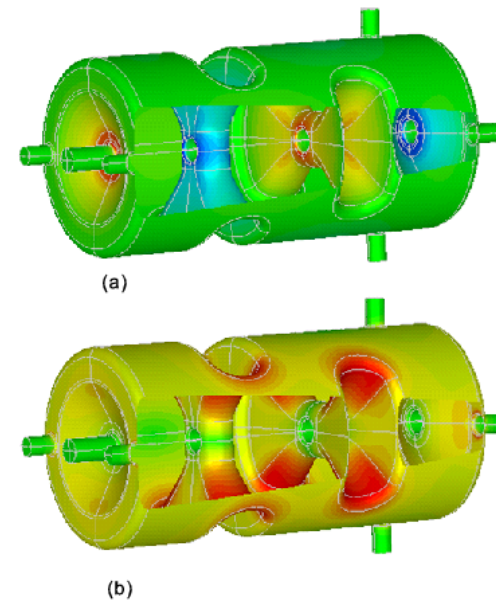


Figure 8: (a) Surface electric field and (b) surface magnetic field for the 500 MHz, velocity of light double spoke cavity.

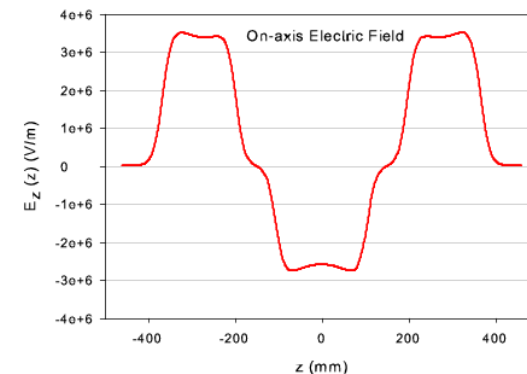


Figure 9: Longitudinal electric field of a single 500 MHz double spoke cavity.

Parameter	Value	Units
Average Kinetic Energy	1.99	MeV
Bunch Charge	10	pC
Longitudinal distribution	Uniform	
RMS bunch length	2.0	mm
p_z distribution	Uniform	
RMS energy spread	0.6	keV
Radial distribution	Uniform	
RMS bunch radius	1.5	mm
p_r distribution	Uniform	
Normalized radial emittance	0.1	π mm-mrad

Table 10: Parameters of Electron Bunch in Beam for Initial Simulations

3.3 Design and Tracking

The design of the linac was evaluated using results generated by the ASTRA particle tracking simulation code. These results were generated by tracking an electron bunch through the electromagnetic field map of the SRF spoke cavity generated by CST. Initially, this bunch was defined by the properties specified in Table 10. Later, this bunch was defined by the results of tracking a bunch with properties specified in Table 4 through the electromagnetic field map of the gun generated first by CST, then Superfish.

The linac is preceded by a superconducting RF injector gun that accelerates an electron bunch produced by a cathode. While the gun has been addressed in Section 2, the transition of the electron bunch from the gun to the linac has significant implications to the design of the linac, so the details of the determining the operating gradient of the gun are addressed here.

At this point, the lack of emittance compensation will be addressed. The purpose of emittance compensation is to transform a phase space distribution such that the shape it makes is an invariant envelope. Phase space distributions to which this is most commonly applied have a significant “bowtie” shape [21]. From Fig. 7, it can be seen that this is not the case. Passing this distribution through a solenoid, the typical tool for this purpose, does not significantly change the distribution as it travels down the beam line through a drift. Leaving a drift in the beam line between the gun and the first cavity of the linac merely allows space charge to have a detrimental impact on the transverse emittance. Additionally, passing through a solenoid has effects on the transverse α and β of the beam; effects which result in the beam behaving poorly as it travels through the linac. Overall, the shape of the transverse phase space has a negligible amount of “bowtie”, especially when compared to the cost of applying compensation.

The two factors that will be discussed in this section are the peak accelerating field of the gun and the distance separating the injector gun and the first cavity. Both of these factors have an impact on space charge, which has an impact on the normalized rms transverse emittance. Space charge is negligible once the electrons are significantly relativistic, so the quicker that the bunch reaches that threshold, the lower the emittance. However, as we increase the the accelerating field, we also increase the peak electric field on the surface. If the peak electric surface field is significantly greater than 35 MV/m, the reliability of the equipment becomes a concern.

Fig. 10 plots the average normalized rms transverse emittance at both the exit of the injector gun and the linac as a function of the average kinetic energy of the electron bunch exiting the gun. The peak electric surface field associated with the average kinetic energy of the electron bunch out of the gun is shown at the top of the graph. To provide a suitable basis of comparison, in each simulation the strength of the cavities in the linac were scaled to produce an average kinetic energy of 25 MeV at the exit, regardless of the energy coming out of the gun. This figure demonstrates the critical point that though a relativistic electron bunch exits the gun, there is still an increase of transverse emittance within the linac. For electron bunches of less than 2.1 MeV average kinetic energy, the amount of transverse emittance gained in the linac decreases linearly as the energy of the electron bunch out of the gun increases. For bunches of higher energy, both the transverse emittance out of the gun and the amount of transverse emittance gained in the linac increases, but as running the gun in that regime would result in a peak electric surface field significantly

greater than 35 MV/m, the causes of this effect will not be addressed here. As a compromise between meeting the specifications of transverse emittance, allowing for some gain of transverse emittance in the bunch compressor, and keeping the peak electric surface field at a reasonable level, the set-up dictates that the average kinetic energy out of the gun is 1.55 MeV, which corresponds to a peak electric surface field of 39 MV/m.

While the beam is relativistic when it leaves the gun, it does not yet have sufficient energy for space charge to be negligible, even at the operating gradient. Consequently, it is desirable to reduce the drift length between the gun and the linac to reduce the effects of space charge. We assume that the minimum iris-to-iris separation between the gun and the first cavity in the linac is 0.158 m, to accommodate all the necessary flanges and bellows. Fig. 11 shows how additional separation increases the average transverse emittance at the exit of the linac for three different kinetic energies out of the gun. The kinetic energies are 1 MeV, 1.4 MeV (which corresponds to a peak electric surface field of 35 MV/m), and 1.55 MeV (the operating gradient). Based on this figure, we can say that the relationship between additional separation and final transverse emittance is linear for any given energy, but the ratio is different for different kinetic energies.

Each cavity is run such that the bunch will gain 5.86 MeV. For the first two cavities, this translates into a peak accelerating field of 13.96 MV/m, with the cavities run on-crest. The last two cavities are run off-crest 6.5° each to “chirp” the beam, which requires the peak accelerating field to be increased to 14.05 MV/m. While the separation between the gun and the first cavity of the linac does significantly impact the relevant parameters of the beam, separations between cavities within the linac do not. Presently, the gun and cavities are contained within three cryomodules. The first contains the gun and one cavity, the second contains two cavities, and the last contains a single cavity. The cryomodules are separated by 0.6 m from iris-to-iris of the cavities adjacent to the gap, and the two cavities within the second cryomodule are separated by 0.32 m iris-to-iris, to account for the connecting flanges and bellows.

Without further adjustment to the set-up, a bunch with the transverse phase spaces and beam spot shown in Fig. 12 arrives at the exit of the linac. Unlike elliptical cavities, spoke cavities have a quadrupole component in the electromagnetic field which could lead to emittance increase. We have explored cavity designs with much reduced quadrupole components [18], but our simulations indicate that the effect of the quadrupole field can be made negligible with a judicious choice of alternate cavity orientation. Several orientations were explored and their transverse optics characterized – see Table 11. Observing the behavior of α and β over the entire length of the linac, it becomes clear that after the second cavity, the beam focuses in y and defocuses in x , not unlike a quadrupole. As quadrupoles are typically paired such that each focuses in one of two orthogonal directions, the cavities were paired off in terms of rotations. In each pair of cavities, the beam would encounter the vertical spoke then the horizontal spoke in the first cavity, before entering the second and encountering the horizontal spoke then the vertical spoke.

However, as the energy of the beam changes as it traverses each pair of cavities, it was uncertain which configuration of rotated and unrotated cavities within the linac would be most advantageous. In this particular case, an unrotated cavity is shown in Fig. 8, where the beam initially encounters the vertical spoke. A rotated cavity is the same figure, rotated 90° either direction around the beam path, so the beam initially encounters a horizontal spoke. Table 11 shows the components of the transverse α and β for the beam at the end of each linac configuration. The configurations listed are all possible combinations of rotated and unrotated cavities. As the objective of this is to determine which configuration minimizes $|\beta_x - \beta_y|$ and $|\alpha_x - \alpha_y|$, it becomes clear that there are four preferable configurations that yield comparable results. These configurations include two rotated and two unrotated cavities, with one rotated and one unrotated cavity as the first two cavities (in any order). The most preferable configuration is with the first and third cavities unrotated, while the second and fourth cavities are.

3.4 Linac Configuration

Table 12 is a concise summary of the linac configuration in its current configuration. The origins of these specifications has been elaborated upon in previous sections. The total length of the accelerator system, consisting solely of the gun, cavities, and the necessary bellows and flanges to connect them, is 4.95 m entirely, though the distance from the cathode to the rear iris of the last cavity is 4.74 m. The characteristics of the beam listed in Table 13 and the distributions shown in Fig. 13 are taken at 26 cm from the final iris.

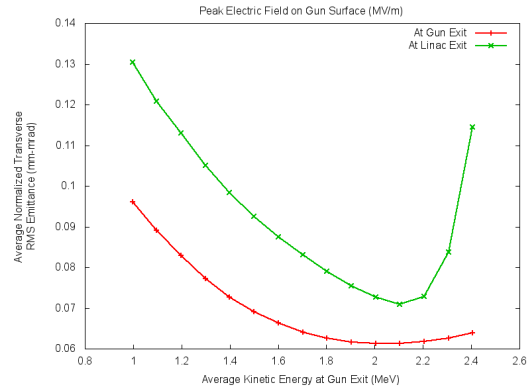


Figure 10: Plot of the average normalized rms transverse emittance at the exit of the gun and linac as a function of the average kinetic energy of the bunch out of the gun and the peak electric surface field of the gun.

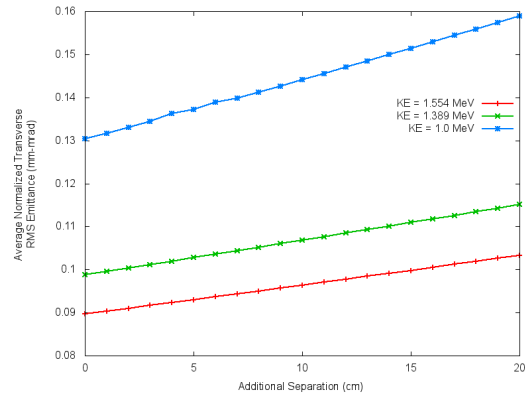


Figure 11: Plot of the average normalized rms transverse emittance at the end of the linac as a function of the distance separating the exit of the injector gun and the entrance of the first cavity for a few different values of the kinetic energy of the electron out of the gun.

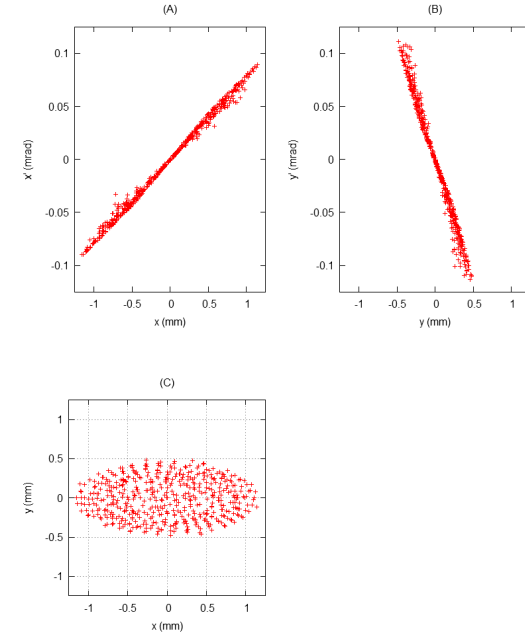


Figure 12: Plots of horizontal (A) and vertical (B) phase spaces and beam spot (C) at exit of linac with no rotated cavities.

Rotated Cavities	β_x	β_y	α_x	α_y
None	181.4	32.77	-13.95	7.695
1	103.7	66.50	-4.984	9.848
2	104.1	71.02	-0.6780	5.878
3	135.8	50.68	-2.381	5.563
4	166.5	37.19	-4.016	5.789
1,2	54.07	127.0	2.528	5.092
1,3	75.51	97.04	1.647	5.041
1,4	94.83	74.72	0.7127	5.879
2,3	72.50	98.76	5.830	0.6094
2,4	94.08	78.63	5.011	1.583
3,4	123.3	56.43	5.069	2.506
2,3,4	64.63	108.1	9.696	-5.327
1,3,4	68.23	107.3	5.775	-0.8282
1,2,4	45.58	140.0	5.460	-2.584
1,2,3	35.60	171.5	5.666	-4.265

Table 11: Transverse Alphas and Betas for Linacs with Different Cavities Rotated

Cryomodule	RF structure	Maximum E_z along beam line	Φ	Iris-to-iris distance from previous structure	Orientation of first spoke
First	Injector Gun	27.972 MV/m	0°	-	-
First	Spoke Cavity	13.959 MV/m	0°	0.158 m	Vertical
Second	Spoke Cavity	13.959 MV/m	0°	0.6 m	Horizontal
Second	Spoke Cavity	14.049 MV/m	6.5°	0.32 m	Vertical
Third	Spoke Cavity	14.049 MV/m	6.5°	0.6 m	Horizontal

Table 12: Summary of Linac Configuration

Parameter	Value	Units
Normalized $\epsilon_{x,rms}, \epsilon_{y,rms}$	0.0912, 0.0883	mm-mrad
Horizontal, vertical RMS beam size	0.4145, 0.3728	mm
RMS bunch length	2.108	mm
RMS energy spread	31.09	keV
Average kinetic energy	25.02	MeV
α_x, α_y	5.011, 1.583	
β_x, β_y	94.08, 78.63	m

Table 13: Beam Properties at Exit of Linac

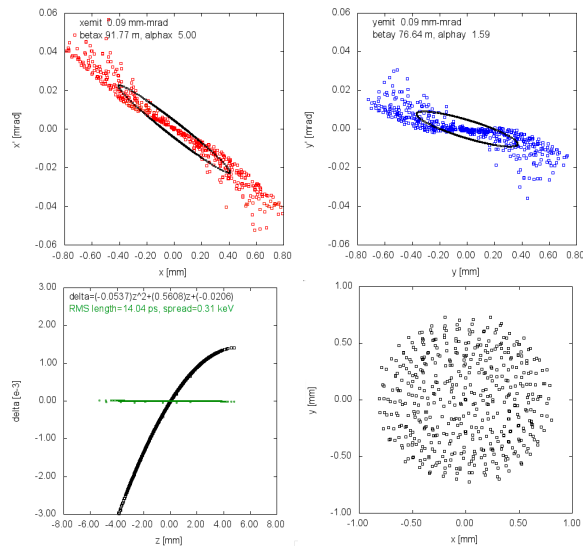


Figure 13: Beam distribution at linac exit, $E=25$ MeV. The green distribution is longitudinal space after ideal curvature removal and bunch rotation, with total longitudinal emittance of 1.3 eV-m, significantly below the 7.5 eV-m design specification. Transverse emittances meet the 0.1 mm-mrad design specification in Table 1.

4 Bunch Compression

Two bunch compressors are being considered for this design; both are purely magnetic achromatic reverse chicanes that permit tunable M_{56} to compress a chirped beam in longitudinal phase space. Final focus is separated from bunch compression in each design to avoid coupling between the bunch compressor and final focus and simplify tuning. This configuration permits straightforward independent tuning of achromaticity, M_{56} , and $\beta_{x,y}$.

Both compressors accomplish tunable compression and final focus with four dipoles for the chicane, and 6-8 independently-powered quadrupoles for optics control. This design is similar to but more compact than other recently constructed compressors in the same energy range [22]; in particular, M_{56} is larger and more independently tunable than traditional chicane compressors.

The triplet final focus section of each compressor focuses to $\beta = 5$ mm and $\alpha = 0$ in both planes, per requirements of Table 1. The triplet provides three degrees of freedom for optics matching; the fourth is provided by a quadrupole at a dispersion zero crossing within the compressor. M_{56} for both designs is tunable over a range of 1.2-1.7m by adjusting the total bend angles and rematching the achromatic constraint.

The first compressor includes 1.5 dispersion function oscillations in the bunch compressor, with a total horizontal phase advance of 3.5π radians. The first and fourth dipoles have the same bend direction, so the overall compressor bends by 105 degrees. The compressor fits in a floor area of $2.8\text{m} \times 3.2\text{m}$ and could be conveniently located in a corner. The floor layout of this compressor section is shown in Fig. 14, and the transverse optics are plotted vs s coordinate in Fig. 15. This compressor is denoted the “ 3π ” compressor, since the total dispersion phase advance is 3π .

The second compressor includes two dispersion function oscillations with a total horizontal phase advance of 4.0π radians, and is thus denoted the “ 4π ” compressor. The central bends and total compression are stronger than in the 3π compressor, but the total bend angle is zero, making it suitable for linear layouts. It fits in a floor area of $2\text{m} \times 3.5\text{m}$. The floor layout and transverse optics of this compressor are shown in Fig. 16. Only three quadrupoles are required within the dispersive region in this design: the central quadrupole provides vertical beta control into the final focus, while the two other symmetrically-placed quadrupoles control horizontal phase advance with minimal impact on overall horizontal focusing.

An additional matching section may be added to the start of the compressor, before and after the first dipole, to match to the linac beam without compromising the phase advance necessary to render the compressor achromatic. In its current configuration, the 3π compressor has an overall $M_{56} = 1.78$ m, which is approximately what is needed to compress an incoming bunch width of $\delta = \Delta p/p_0 = \pm 10^{-3}$ by the incoming bunch length of $z = \pm 2$ mm.

Quadrupoles in both designs are typically 10 cm long, and are consistent in strength (up to 9 T/m) and coil cooling requirements with commercially available air-cooled quadrupoles from various vendors such as the RadiaBeam .BEMQD-01-155-245 air-cooled diamond quadrupole [23].

Further optimization work on the bunch compressors will focus on tunability, chromatic compensation in the final focus, and T_{566} nonlinear longitudinal focusing to correct longitudinal bunch distortion from the linac. T_{566} should be straightforward to independently control to first order with the inclusion of sextupoles at high dispersion locations in the bunch compressor [24]. Beam dynamics considerations will follow those in [25].

We are also considering alpha magnet bunch compression, where the beam is compressed at much lower energy, usually after the gun and before the linac[26]. Alpha magnet compression would eliminate the need for a longer magnetic bunch compression, and for bunch chirping in the linac. However, it is possible that space charge and transverse emittance considerations will preclude this approach from meeting transverse emittance requirements. Previous work [27] indicates significant emittance growth for 20 pC, 2.15 MeV bunches, parameters near our parameters of 10 pC, 1.554 MeV bunches at the RF gun exit. We are in consultation with Mike Borland at Argonne to determine and possibly develop consistent methods to further evaluate alpha magnet beam tracking in the presence of strong space charge.

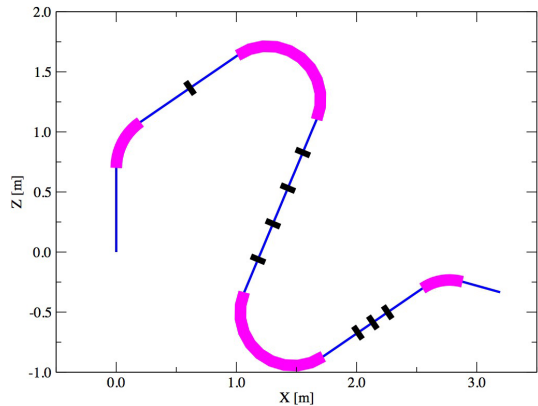


Figure 14: Magnetic bunch compressor floor layout.

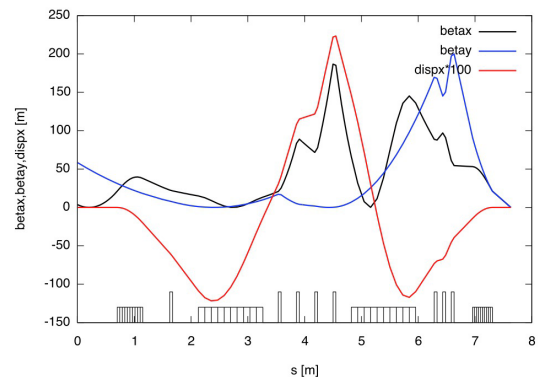


Figure 15: Magnetic bunch compressor optics, including the 3π phase advance of dispersion and integrated low-beta focusing section.

5 Accelerator Systems Performance

5.1 Integrated Tracking

Beam dynamics for the linac were also simulated using ASTRA [8]. ASTRA was developed by DESY and consists of five programs. A list of these programs and a brief description of their capabilities is contained in Table 14. The initial distribution of electrons coming off the cathode was produced using *generator*. This distribution is then tracked through the injector gun and linac cavities. ASTRA tracks particles in 6 dimensions while incorporating space charge. This is accomplished by using a non-adaptive fourth-order Runge-Kutta integration, accounting for both user-defined external fields and the bunch space charge. Using *lineplot*, we can see how different properties of the beam change as they travel through the gun and linac,

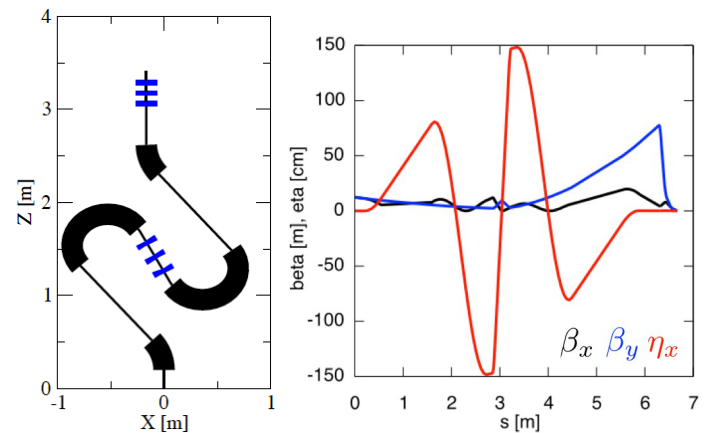


Figure 16: Magnetic bunch compressor footprint (left) and optics (right). The compressor fits within a $2.0\text{m} \times 3.5\text{m}$ space, and provides large dispersion for sextupole chromatic and T_{566} control.

while *postpro* displays the distribution of the bunch at different longitudinal locations along the accelerator system.

Program Name	Brief Description
ASTRA	Tracks particles impacted by internal and external fields
<i>generator</i>	Generates an initial distribution of particles
<i>fieldplot</i>	Displays electromagnetic and space charge fields
<i>lineplot</i>	Displays beam properties as a function of longitudinal position
<i>postpro</i>	Displays phase space distributions

Table 14: Descriptions of Programs included in ASTRA Program Package

Electromagnetic fields for each cavity and injector gun design were exported to text files from CST or Superfish. These text files were subsequently parsed into the format required by ASTRA. The distribution of electrons was tracked through different designs of the gun and cavities by ASTRA. The phase of each cavity was automatically defined by ASTRA such that the energy gain was maximized at zero degrees. Each design was then evaluated based on the properties of the electron beam after it exited the final cavity. Among the relevant properties were normalized transverse emittance, longitudinal emittance, energy spread, bunch length, and beam size.

The parsing of electromagnetic field maps supplied by CST and Superfish were achieved by various python scripts. In the case of CST field maps, the data merely had to be rearranged, and in the case of the magnetic field, multiplied by μ_0 . The Superfish field data was initially exported in cylindrical coordinates. The cylindrical coordinates were transformed into Cartesian coordinates, but these Cartesian coordinates did not have a uniform step size. The coordinates were then interpolated to fill in the necessary coordinates to produce a uniform step size. Both linear and spline interpolations were tried, and the results were consistent to first order.

It was necessary to verify that the generated simulation results were independent of the step and mesh sizes of the electromagnetics fields. This included the step size of data exported by CST, the step size of data exported by Superfish, the step size of the Cartesian grid to which the Superfish data is translated, and the mesh sizes of both the CST and Superfish simulations. Overall, each step and mesh size was determined to

be sufficiently small when simulations run with reduced sizes had no significant differences in results. While a similar consideration might have been appropriate for the Runge-Kutta step-size in ASTRA, ASTRA generates warning messages when the step-size is too large and risks producing incorrect results. This allows the user to re-run the simulation with a more appropriate step-size. A similar warning is given by Superfish for the mesh size.

At the end of the simulation, a text file is produced that contains the six-dimensional coordinate information for all of the electrons. The first line is reserved for the “reference” particle. The longitudinal position and longitudinal momentum of all other electrons are relative to the longitudinal position and momentum of the reference particle. Using a python script, the relative coordinates are translated into absolute coordinates, which are recorded in place of the relative coordinates. This distribution of electrons is then passed to *elegant* via a perl parser to be passed through the bunch compressor and beam transport system.

References

- [1] T. Satogata et al., “Compact Accelerator Design for a Compton Light Source”, WEPWA078, Proc. of the 4th International Particle Accelerator Conference (IPAC2013), Shanghai, China (2013).
- [2] G. Krafft and G. Priebe, “Compton Sources of Electromagnetic Radiation”, Reviews of Accelerator Science and Technology Vol 3 Issue 1 (2010), pp. 147-163, available freely at <http://www.worldscinet.com/rast/03/0301/free-access/S1793626810000440.pdf>.
- [3] W.S. Graves et al., “MIT Inverse Compton Source Concept”, Nucl. Instr. Methods Phys. Res. A **608**, S103 (2009).
- [4] G. Krafft, “Requirements for a Compton Source”, Jefferson Lab Tech Note, received 14 June 2012.
- [5] J.R. Harris et al., “Design and Operation of a Superconducting Quarter-Wave Electron Gun”, PRST:AB **14**, 053501 (2011).
- [6] Computer Simulation Technology website, <http://www.cst.com>.
- [7] Poisson Superfish, <http://laacg1.lanl.gov/laacg/services/download.sf.phtml> (2011).
- [8] K. Flottman, “A Space-Charge Tracking Algorithm”, DESY, <http://www.desy.de/~pyf10> (2011).
- [9] C.S. Hopper, R.G. Olave, and J.R. Delayen, “Superconducting Single-Spoke Cavities for High-Velocity Applications”, WEPWO079, Proc. of the 4th International Particle Accelerator Conference, Shanghai, China (2013).
- [10] C.S. Hopper, R.G. Olave, and J.R. Delayen, “Development of Spoke Cavities for High-Velocity Applications”, WEPPC103, Proc. of the 3rd International Particle Accelerator Conference (IPAC2012), New Orleans, USA (2012).
- [11] C.S. Hopper and J.R. Delayen, “Design of Superconducting Spoke Cavities for High-Velocity Applications”, MOPO033, Proc. of the 15th International Conference of RF Superconductivity (SRF2011), Chicago, IL (2011).
- [12] J.R. Delayen, “Applications of Spoke Cavities”, TU302, Proc. of the 2010 Linac Conference (LINAC2010), Tsukuba, Japan (2010).
- [13] J.R. Delayen, S.U. DeSilva, and C.S. Hopper, “Design of Superconducting Spoke Cavities for High-Velocity Applications”, TUP100, Proc. of the 2011 Particle Accelerator Conference (PAC2011), New York, New York (2011).
- [14] J.R. Delayen, C.S. Hopper, and R.G. Olave, “Design of Low-Frequency Superconducting Spoke Cavities for High-Velocity Applications”, MOPC121, Proc. of the 2nd International Particle Accelerator Conference (IPAC2011), San Sebastian, Spain (2011).
- [15] D. Gorelov, J.R. Delayen, C.S. Hopper, R.G. Olave, S. DeSilva, et al. “Development of a Superconducting 500 MHz Multi-Spoke Cavity for Electron Linacs”, WEPPC084, Proc. of the 3rd International Particle Accelerator Conference (IPAC2012), New Orleans, Louisiana (2012).
- [16] C.S. Hopper, J.R. Delayen, and R. Olave, “Higher Order Mode Properties of Superconducting Two-Spoke Cavities”, MOPO022, Proc. of the 16th International Conference on RF Superconductivity (SRF2011), Chicago, Illinois (2011).
- [17] C.S. Hopper and J.R. Delayen, “Multipacting Analysis of High-Velocity Superconducting Spoke Resonators”, SUPB026, Proc. of the 2012 Linac Conference (LINAC2012), Tel Aviv, Israel (2012).
- [18] R.G. Olave, J.R. Delayen, and C.S. Hopper, “Multipole Expansion of the Fields in Superconducting High-Velocity Spoke Cavities”, MOPB072, Proc. of the 2012 Linac Conference (LINAC2012), Tel Aviv, Israel (2012).
- [19] Jefferson Lab cryo-group, “Cryogenics at Jefferson Lab”, Cryo tutorial at Jefferson Lab, Jan. 25, 2011.
- [20] F. He, “Design of a $\beta = 1$ Double Spoke Cavity for the BES-CLS ICS Light Source”, ICFA Workshop on Future Light Sources, Newport News, VA (2012).
- [21] B.E. Carlsten, “New Photoelectric Injector Design for the Los Alamos National Laboratory XUV FEL Accelerator”, Nucl. Instrum. Methods A **285**, 313 (1989).
- [22] J. Saisut et al., “Construction and Performance of the Magnetic Bunch Compressor for the THz Facility at Chiang Mai University”, Nucl. Instr. and Meth. Phys. Res. A **637** (2011), S99-S106.
- [23] RadiaBeam website, http://www.radiabeam.com/upload/catalog/pdf/136555330020130319_EMQD-01-155-245.pdf.
- [24] R. J. England, “Longitudinal Shaping of Relativistic Bunches of Electrons Generated by an RF Photoinjector”, Ph.D. Thesis, UCLA (2003).
- [25] C.R. Prokop, P. Piot, B.E. Carlsten, and M. Church, “Beam Dynamics Performances and Applications of a Low-Energy Electron-Beam Magnetic Bunch Compressor”, arXiv:1302.0726v1 (4 Feb 2013).
- [26] M. Borland, Ph.D. Thesis, Stanford University (1991).
- [27] H. Hama et al., “Space Charge Effect for Short Electron Bunches in an Alpha Magnet”, TUPPH029, Proc. of the 2008 FEL Conference (FEL2008), Gyeongju, Korea (2008).